

Periodic Dielectric Metasurfaces with High-Efficiency, Multiwavelength Functionalities

David Sell, Jianji Yang, Sage Doshay, and Jonathan A. Fan*

Metasurfaces are thin-film optical devices for tailoring the phase fronts of light. The extension of metasurfaces to multiple wavelengths has remained a major challenge, and existing design techniques do not yield devices with high efficiency. This study reports a new design method, based on inverse freeform optimization, that enables high-efficiency, multiwavelength metasurfaces. Using an iterative optimization solver, this study incorporates multiple wavelength responses into wavelength-scale design domains in a straightforward and automated manner. In principle, this method can readily scale to a very large number of wavelengths. As a proof of concept, this study designs and characterizes periodic transmissive metasurfaces, made from silicon, that deflect N different incident near-infrared wavelengths to N unique diffraction orders. The theoretical and experimental efficiencies of these devices scale as $1/N^{0.5}$, which is significantly better than current state-of-the-art devices. The implementation of large-angle, broadband blazed grating devices is also demonstrated. This study envisions that this inverse design method can generalize to high-performance, multiwavelength, aperiodic devices, and that it serves as a potential route to broadband metasurfaces.

Metasurfaces are thin-film optical devices that use nanoscale geometric designs to shape the wavefront of electromagnetic waves. Their ability to specify nearly arbitrary phase responses enables a broad range of applications, including holograms,^[1] lenses,^[2,3] retroreflectors,^[4] beam steering devices,^[5] spectroscopic elements,^[6] and imaging filters.^[7,8] Conventionally, these devices utilize subwavelength-scale nanoresonator or nanowaveguide building blocks, which have amplitude and phase responses tailored to a target wavelength.^[9] These building blocks are then stitched together into macroscopic arrays to produce a desired wavefront response. For many current realizations of metasurfaces, devices are designed for a single input wavelength.

D. Sell, S. Doshay
Department of Applied Physics
Stanford University
Stanford, CA 94305, USA

Dr. J. Yang, Prof. J. A. Fan
Department of Electrical Engineering
Stanford University
Stanford, CA 94305, USA
E-mail: jonfan@stanford.edu

 The ORCID identification number(s) for the author(s) of this article can be found under <https://doi.org/10.1002/adom.201700645>.

DOI: 10.1002/adom.201700645

There is tremendous interest in generalizing the design of metasurfaces to include multifunctional responses, where a single “function” is taken to mean an individual wavefront response specified for an incident plane wave with a distinct polarization, wavelength, and direction. Multifunctional metasurfaces represent a versatile class of optical devices that enable an expanded range of applications compared to their single-function counterparts. For example, multifunctional devices that produce the same wavefront response for different incident wavelengths are key components in aberration-corrected, multispectral imaging systems. Devices that produce distinct responses for different incident wavelengths are the basis for wavelength-multiplexed beam steering, focusing, and filtering applications.

There currently exist design methods to produce high-efficiency, dual-function metasurfaces using polarization-based multiplexing schemes. These approaches incorporate anisotropy in the subwavelength-scale metasurface building blocks to produce polarization-dependent phase responses.^[10] They have been used to realize dual-wavelength metalenses^[11,12] and dual-function holograms.^[13,14]

It is less straightforward to design multifunctional metasurfaces without exploiting the polarization degree of freedom. For devices that support distinct functions for different wavelengths with the same polarization, current design strategies include sectoring,^[15–17] interleaving,^[16–18] and the brute-force searching of subwavelength building blocks.^[19–21] In the sectoring and interleaving approaches (Figure 1a,b), devices are subdivided into regions that are individually designed for a single wavelength. Sectoring device regions are larger than a wavelength, while interleaved device regions are subwavelength in scale. The brute-force search approach utilizes a library of subwavelength-scale building blocks, which each possess multiwavelength responses (Figure 1c). Upon searching through this library, building blocks with the desired responses are identified and stitched together.

While these methods each provide a pathway for multiplexing functions, the efficiencies of the resulting multifunctional devices are limited. For N total input wavelengths, sectoring devices possess a maximum average efficiency of $1/N$ at each wavelength. Interleaved devices have theoretical efficiencies that surpass the $1/N$ limit, but experimental demonstrations

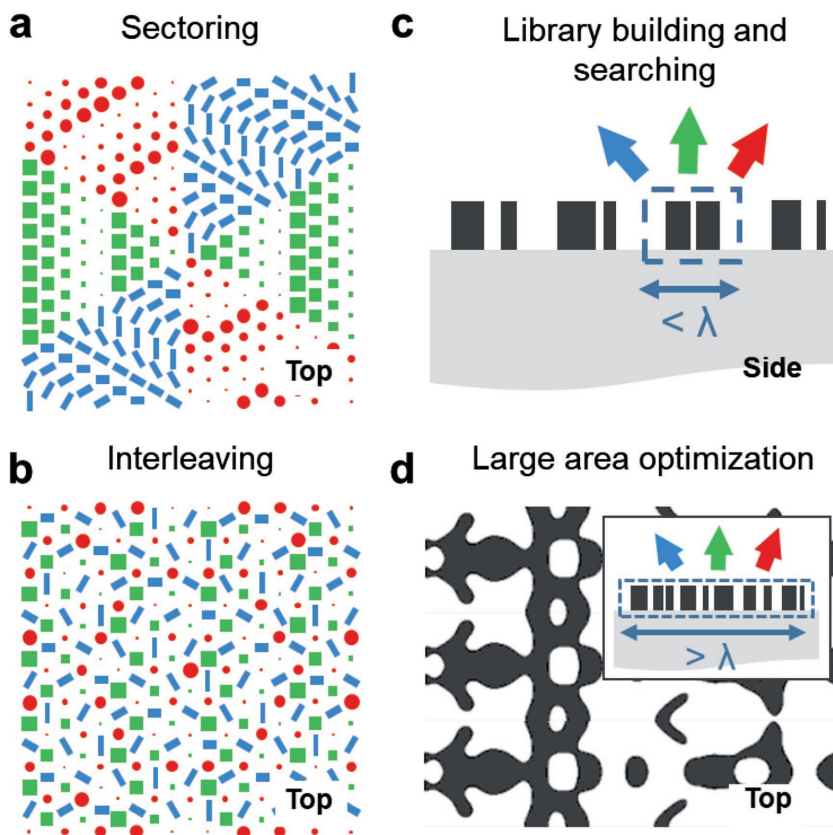


Figure 1. Design approaches to multifunctional metasurfaces. a) The sectoring approach combines three functions by stitching together wavelength-scale regions, each designed for a single function, represented by different colors. b) The interleaving approach combines three functions by stitching together subwavelength-scale elements. c) The searching approach utilizes a library of multifunctional, subwavelength-scale structures. d) The direct optimization of multifunctional, wavelength-scale regions is the subject of this report.

have yet to break this limit.^[16,18] For the brute-force search approach, it becomes increasingly difficult to identify efficient building block designs as the number of functions increases, due to the limited design space provided by subwavelength-scale structures. Optical transmission devices constructed in this way do not yield high efficiencies.^[19–21]

In this Article, we demonstrate wavelength-multiplexed silicon metasurfaces that support significantly higher efficiencies than the current state-of-the-art. Our method uses adjoint-based inverse design, which is an iterative optimization procedure that can produce high-performance nanophotonic devices comprising nonintuitive patterns.^[22–25] In an initial study, we showed that adjoint-based optimization can be used to produce large-angle, high-efficiency metasurface deflectors that can respond to one and two wavelengths.^[26–28] As we analyze here, this design approach can scale to the optimization of N functions in a straightforward manner. As an illustration, we design and demonstrate periodic metasurfaces, i.e., metagratings, which can steer incident near-infrared plane waves to different diffraction orders based on wavelength (Figure 2a). It is not clear or obvious how the efficiency scales with number of functions or wavelengths in topology-optimized devices. We find that the theoretical and experimental efficiencies of these

wavelength splitters surpass $1/N$ by a wide margin. While our analysis here is limited to periodic metasurfaces that deflect light to specific diffraction angles, we anticipate that these results can generalize to aperiodic devices that can steer light to arbitrary angles.

One feature of our approach is that we directly optimize the multiwavelength responses of a full period of the metagrating, which is larger than a wavelength. By optimizing wavelength-scale regions, as opposed to subwavelength-scale building blocks, we access a larger overall design space. Another feature is that our method optimizes for topology and is not limited to a predefined number of discrete shapes, which is a common restriction of other metasurface optimization techniques.^[29,30] The curvilinear and interconnected geometries produced with our design technique incorporate intricate optical mode coupling dynamics that enhance device efficiency.^[27] We also note that our devices are based on low loss, high refractive index materials. In contrast to multifunctional devices based on plasmonics,^[31] our devices do not suffer from material absorption.

Our inverse design method begins with a dielectric slab consisting of a random continuum of refractive indices with values ranging between air (n_{air}) and polycrystalline silicon (n_{silicon}). The values of these refractive indices are $n_1(\mathbf{r})$, where the subscript “1” represents the starting point for our optimization (i.e., iteration 1). \mathbf{r} spans our design domain, which is the x - y space of a single

period of our metagrating (coordinates are in Figure 2a). Over the course of multiple iterations, the refractive indices at each point in the design domain are gradually “pushed” toward n_{air} or n_{silicon} , until the design domain finally converges to a device consisting of discrete air and silicon features (Figure 2b).

The goal of each iteration is to improve the Figure of Merit (FoM), which is a single-valued number that captures our desired design objective. For a single-wavelength metagrating that deflects an incident plane wave to a particular desired diffraction order, a simple and effective choice for the FoM is: $\text{FoM} = T$, where T is the transmission efficiency into the target diffraction order. As the transmission efficiency improves, the FoM increases monotonically. As such, for the m th iteration, the determination of whether $n_m(\mathbf{r})$ is increased or decreased at a particular \mathbf{r} is based on whether that index change improves the FoM.

Mathematically, these changes in refractive index are linked to the FoM through the gradient $G(\mathbf{r}) = \partial \text{FoM} / \partial n(\mathbf{r})$, which is used to compute $\Delta n(\mathbf{r})$ such that $n_{m+1}(\mathbf{r}) = n_m(\mathbf{r}) + \Delta n(\mathbf{r})$. We calculate this gradient using the adjoint method, which is discussed in detail in ref. [23]. For a single-wavelength, single-function device, $G(\mathbf{r}) \propto \frac{n(\mathbf{r})}{\lambda^2} \text{Re} \{ \mathbf{E}^{\text{fwd}}(\mathbf{r}) \cdot \mathbf{E}^{\text{adj}}(\mathbf{r}) \}$. Here, $\mathbf{E}^{\text{fwd}}(\mathbf{r})$ is the electric field in the domain, as calculated by the forward

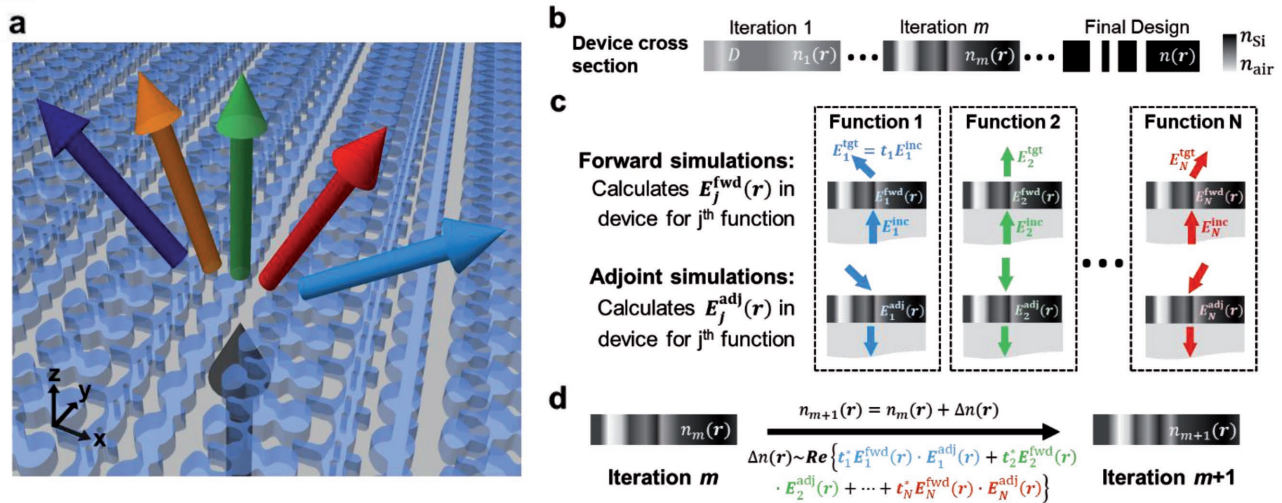


Figure 2. Description of our metasurface design process. a) Illustration of a metagrating supporting five functions. Five normally-incident plane waves, each with a different wavelength, transmit through the device and deflect to differing diffraction order channels in the x - z plane with high efficiency. b) Summary of our iterative design procedure based on adjoint optimization. For the first iteration, our design domain D consists of a refractive index continuum $n_1(r)$ with values between n_{Si} and n_{air} . Over the course of multiple iterations, these refractive index values are adjusted until they finally converge to $n(r)$, which has values of either n_{Si} or n_{air} . c) Schematics of the simulations performed during an individual iteration. Two simulations are performed for each of the N functions, a forward and an adjoint simulation. d) Parameters from the forward and adjoint simulations in (c) are used to specify $\Delta n(r)$, which is added to $n_m(r)$ after the m th iteration.

simulation (i.e., illuminating the device with a normally incident plane wave), and t_j is the complex transmission efficiency into the target direction. $E^{\text{adj}}(r)$ is the adjoint electric field in the domain, as calculated by the adjoint simulation (i.e., illuminating the device with a plane wave from the target diffraction order direction). The values that we use for $E^{\text{fwd}}(r)$ and $E^{\text{adj}}(r)$ correspond to electric fields averaged over the thickness of the device. With the adjoint method, $G(r)$ for the entire design region can be calculated using only two electromagnetic simulations per iteration.^[24]

A key aspect of our method is that it can readily extend to the incorporation and optimization of multiple functions. We approach this design problem by defining a new FoM that sums the individual FoMs for each function. As the overall functionality of the device improves over the course of the iterative optimization process, this modified FoM will increase monotonically. For our case of a metagrating splitter that deflects N input wavelengths to N different diffraction orders, our new FoM is expressed as

$$\text{FoM} = \sum_{j=1}^N c_j T_{u_j}(\lambda_j) \quad (1)$$

where $T_{u_j}(\lambda_j)$ is the diffraction efficiency of wavelength λ_j into diffraction order u_j . c_j is a weighting factor used to indicate how much importance is given to each function. In the case where the weighting factors are the same for each wavelength, the gradient $G(r)$ has the form

$$G(r) \propto \sum_{j=1}^N \frac{n(r)}{\lambda_j^2} \text{Re} \{ t_j^* E_j^{\text{fwd}}(r) \cdot E_j^{\text{adj}}(r) \} \quad (2)$$

A schematic of our evaluation of t_j , $E_j^{\text{fwd}}(r)$, and $E_j^{\text{adj}}(r)$ is in Figure 2c. Our pathway to generalizing our design process to

multiple functions is clear: for each iteration, we perform a forward and adjoint simulation for each individual function and use the calculated fields in the design domain to define $G(r)$, which specifies $\Delta n(r)$ (Figure 2d). Our method readily extends to a large number of functions (i.e., unique optical responses for incident planes of differing polarization, wavelength, or angle of incidence), which is beyond the capability of conventional metasurface design approaches.^[9]

We demonstrate the utility of adjoint-based optimization by analyzing a series of metagrating splitters that steer N normally-incident plane waves, each with unique wavelengths, into N distinct diffraction orders. The target diffraction orders for each wavelength are chosen to create a large angular spread between adjacent wavelengths. We analyze the cases of N equal to 2, 3, 4, and 5, and the polarization of the incident waves is fixed to be either TE ($|E| = E_y$, see Figure 2a for axes) or TM ($|H| = H_y$). The grating thickness and period are 325 and 2500 nm, respectively, and the wavelengths range from 900 to 1300 nm and are evenly spaced in frequency. Light diffraction only takes place in the x - z plane as the grating period along the y direction is subwavelength in scale. These devices are designed to include robustness to geometric erosion and dilation,^[26,32] which we incorporate into the optimization process to mitigate the impact of experimental fabrication errors in device efficiency. To perform the forward and adjoint electromagnetic simulations, we use rigorous coupled-wave analysis (RCWA),^[33] which is a computation technique that supports fast and accurate calculations for periodic systems.

The device layouts of these wavelength splitters for differing N are summarized in Figure 3, together with a plot of their theoretical efficiencies. In each case, the designs are curvilinear, nonintuitive, and have no clearly associated length scale. The absolute and relative efficiencies represent the fraction of light

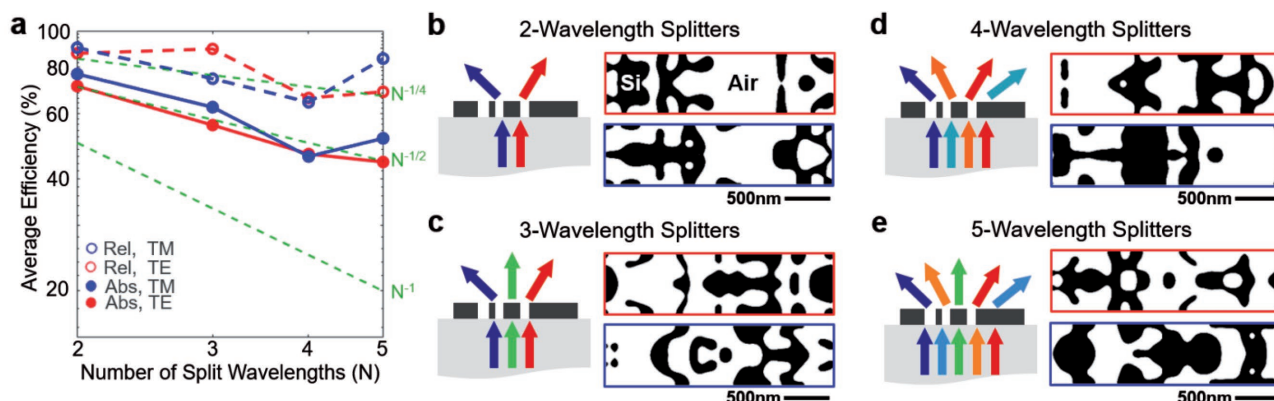


Figure 3. Theoretical analysis of multiwavelength metagrating splitters. a) Plot of the device efficiency, averaged for each wavelength, as a function of number of wavelengths (N). Devices designed for TE- and TM-polarized incident waves are denoted by red and blue colors, respectively. The solid lines represent absolute efficiencies, and the dashed lines represent relative efficiencies. The dashed green lines are reference curves showing the $1/N$, $1/N^{0.5}$, and $1/N^{0.25}$ scaling trends. b–e) Schematics and top views of a single period of the optimized metagratings. Devices designed for TE- and TM-polarized incident waves are outlined with red and blue lines, respectively. Black represents silicon and white represents air. Wavelengths and target diffraction orders (in parentheses) for each device are as follows: (b) 900 nm (–2), 1300 nm (+1); (c) 900 nm (–2), 1064 nm (0), 1300 nm (+1); (d) 900 nm (–2), 1003 nm (+2), 1132 nm (–1), 1300 nm (+1); (e) 900 nm (–2), 975 nm (+2), 1064 nm (0), 1170 nm (–1), 1300 nm (+1).

transmitted to the desired diffraction channel, normalized to the magnitudes of incident light and total transmitted light, respectively.

In all cases, the calculated efficiencies are high and well above the $1/N$ benchmark. As the number of wavelengths being split increases, the average efficiency decreases due to the challenge of optimizing for multiple distinct functions within the same device region. Fits to the average absolute efficiencies as a function of N (Figure 3a, solid lines) show that these device efficiencies scale approximately as $1/N^{0.5}$, displaying a much smaller drop-off than that featured in the $1/N$ benchmark. The average relative efficiencies as a function of N are even better and scale approximately as $1/N^{0.25}$. Unexpectedly, the efficiencies of the five-wavelength splitter are generally larger than that of the four-wavelength splitter. We speculate two potential causes. First, the four-wavelength splitter does not include a 0th-order diffraction component, which may impose a constraint on the design space. Second, the specific wavelengths and diffraction orders chosen in the five-wavelength splitter may be particularly amenable to high-efficiency design.

The simulated electromagnetic fields within and above the TM-polarized five-wavelength splitter are plotted in Figure 4 for each target wavelength. The fields above the device show clearly defined wavefronts propagating in the direction of the desired diffractive order, which is indicative of the large relative efficiencies supported for each function in the device. The field plots within

the metagrating show that distinct modes are responsible for high-efficiency deflection for each wavelength. These modes possess complex spatial profiles and utilize different regions

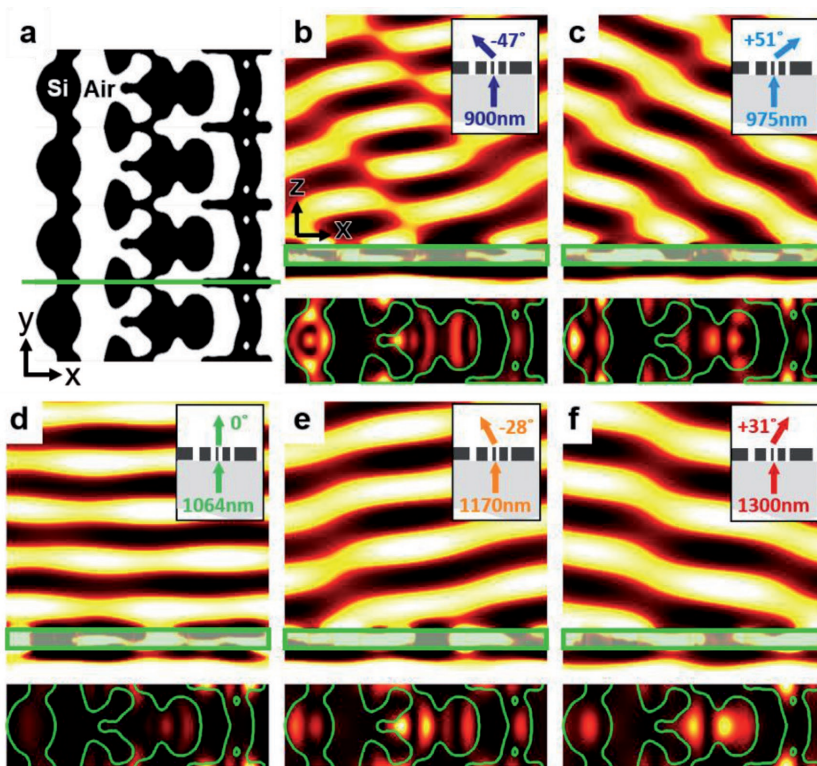


Figure 4. Simulated fields of the five-wavelength splitter designed for TM-polarized incident waves. a) Top view schematic of four periods of the device. Black represents silicon and white represents air. The green solid line represents the cross-sectional plane used to evaluate the fields in (b)–(f). b–f) Plots of $|E|^2$ in the x - z plane at each target wavelength. The translucent green box represents the metasurface cross-section. Top-right insets: Schematics showing the incident wavelength and target deflection angle. Bottom insets: $|H|^2$ cross-sectional plots taken from the x - y plane located at the metagrating midpoint. The green outlines delineate the air-silicon boundaries.

of the silicon structure depending on the incident wavelength. A mode analysis^[27,34] of the metagrating is summarized in Figure S8 in the Supporting Information and shows quantitatively that different sets of modes are utilized for light deflection for different target wavelengths. Furthermore, the modes are strongly dispersive and have spatial profiles and effective refractive indices that vary with wavelength. These mode profiles and scattering dynamics are highly intricate and can only be properly implemented using high-performance numerical optimization techniques.^[27]

To experimentally demonstrate our metagratings, we fabricate and optically characterize a set of TM-polarized wavelength splitters designed for 2–5 input wavelengths. The experimental details are in the Experimental Section. To summarize, we prepare the samples by growing polycrystalline silicon films on a silicon dioxide substrate, followed by patterning with electron beam lithography and reactive ion etching. To characterize the devices, we weakly focus a light beam from a tunable white light laser source onto our samples and measure the transmitted power as a function of angle using a detector mounted on a goniometer.

Scanning electron microscopy (SEM) images and experimental angular deflection data for two- and five-wavelength splitters are presented in Figure 5. SEM images and experimental data of the three- and four-wavelength splitters are in the Supporting Information (Figures S1 and S2). The SEM images of these devices show that the designs (Figure 3) were reproduced in the lithographic patterning steps with high fidelity. The experimental data show peaks in efficiency at the intended diffraction angle for each target wavelength (Figure 5b,f), indicating that each designed optical function is captured with high relative efficiencies in our fabricated devices. A plot of average relative efficiency versus N is in

Figure S3 in the Supporting Information and shows that these device efficiencies scale as $0.9/N^{0.5}$, which is considerably more gradual than the $1/N$ benchmark.

Compared to the theoretical relative efficiencies plotted in Figure 5c,g, the experimental efficiencies are, on average, $\approx 20\%$ lower. These deviations between experimental and theoretical efficiencies are due in part to fabrication errors, where pattern distortions during electron beam exposure, development, and etching can manifest and degrade device performance. These deviations are also due to the finite bandwidth of our tunable white light laser source after filtering. If the bandwidth of high-efficiency operation in our device is less than the bandwidth of our filtered light source, the measured device efficiency will be lower than the actual value. For our devices, the bandwidth of high-efficiency operation at certain target wavelengths can be very narrow (Figure S4, Supporting Information).

Our inverse design scheme can generalize to the optimization of a very large number of functions. As a proof-of-concept, we design and experimentally characterize a broadband blazed metagrating that deflects normally-incident TM-polarized light, with wavelengths ranging from 1000 to 1300 nm, to the +1 diffraction order. For our grating period of 1556 nm, the span of deflection angles ranges from 40° to 57° . To design this device, we optimize for 20 incident wavelengths that are equally spaced in wavelength throughout our target bandwidth. The theoretical efficiency plots in Figure 6, which are rigorously calculated with high spectral resolution, show that even though the device is optimized at discrete wavelengths, those wavelengths are sufficiently close together to produce a high-efficiency broadband response. We note that there do exist a few sharp dips in efficiency at wavelengths located between our discrete optimization wavelengths, which are unaccounted for in our design process. These features can be reduced by decreasing

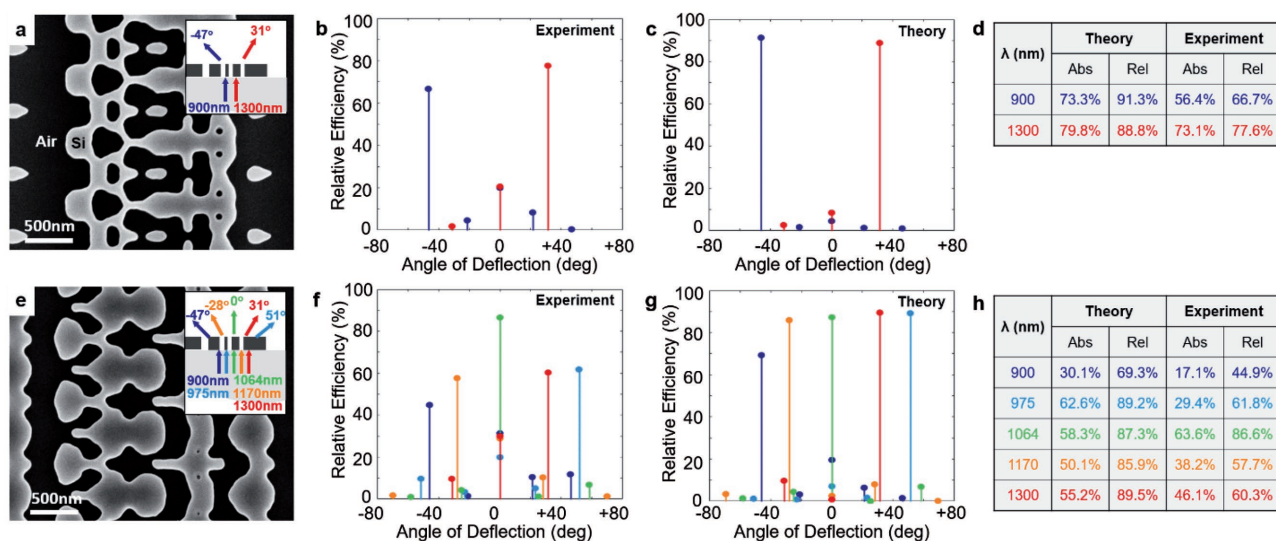


Figure 5. Experimental characterization of two- and five-wavelength splitters. a) Scanning electron microscopy images of a two-wavelength splitter designed for TM-polarized incident waves. Inset: Schematic showing the target wavelengths and deflection angles for the device. b) Experimental plot of the measured relative efficiencies for the two-wavelength device. The different colors in the plots represent different target wavelengths and correspond to the colors in the inset of (a). c) Plots of theoretically calculated relative efficiencies for the two-wavelength device. d) Summary of the theoretical and experimental efficiencies for the two-wavelength splitters. e–h) Scanning electron microscopy images and efficiency data of the five-wavelength splitter, following the same format as (a–d).

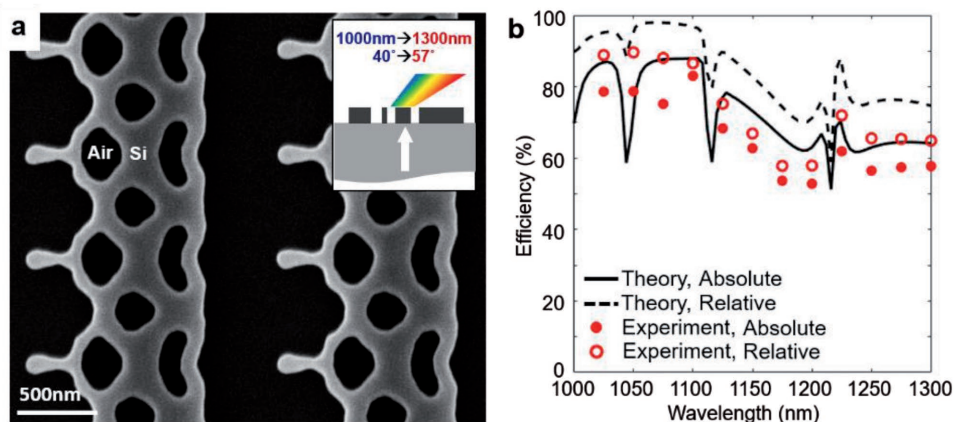


Figure 6. Experimental characterization of a broadband blazed metagrating. a) Scanning electron microscopy image of a blazed metagrating operating between 1000 and 1300 nm for TM-polarized normally-incident waves. Inset: Schematic summarizing the range of incident wavelengths and target deflection angles. b) Plot of the theoretical and experimental efficiencies versus wavelength for the device. The theoretical absolute and relative efficiencies are represented by the black solid and dashed lines, respectively. The experimentally-measured absolute and relative efficiencies are represented by the red dots and circles, respectively.

the spacing between optimization wavelengths in the design process. An SEM image of the device and the experimental absolute and relative efficiencies are also presented in Figure 6, and the data generally agree well with the theoretical curves. The experimental absolute efficiencies are approximately 10% lower than those calculated theoretically, indicating that these devices are relatively robust to fabrication imperfections. Theoretical and experimental results for similar devices operating for TE and dual-polarization inputs are in Figures S5–S7 in the Supporting Information.

In summary, we show that high-efficiency, multifunctional periodic metasurfaces can be designed and implemented using adjoint-based inverse design. With this technique, we directly optimize device regions that span wavelength-scale dimensions, which allows us to access a large design space and engineer modes with complex spatial profiles and dynamics within the device.^[26,27] Our devices, which deflect N incident plane waves of differing wavelength to N unique diffraction orders, support average absolute device efficiencies that theoretically and experimentally scale as $1/N^{0.5}$, which far surpasses the $1/N$ benchmark that is typical of current state-of-the-art approaches. Further improvements to the design process are likely to further surpass this scaling relation. While the device designs here are limited to periodic structures, due to our use of an RCWA electromagnetics solver, we envision that topology optimization can be applied to realize high-performance, multifunctional aperiodic metasurfaces, when used in conjunction with electromagnetics solvers that can accommodate nonperiodic layouts.

Experimental Section

Sample Preparation: To prepare the samples, a 325 nm thick layer of polycrystalline silicon (p-Si) was grown using chemical vapor deposition, followed by a 30 nm thick silicon dioxide hard mask on a clean fused silica substrate. The p-Si layer was patterned using a 100 nm layer of CSAR 92 electron beam resist together with a layer of Electra 92 conductive polymer to prevent charging. The metasurface devices, which each

were circular shapes with 200 μm diameters, were patterned using a JEOL JBX 6300 electron beam lithography system. The samples then underwent a two-step reactive ion etch. The first etch used the CSAR 92 as a mask to etch the 30 nm thick silica hard mask, and the second etch used an etch chemistry that was highly selective to oxide to etch the 325 nm thick p-Si layer.

Device Characterization: To characterize the metagratings, a tunable white light laser source was used, which was tuned to a desired wavelength, polarized with a near-IR polarizer, and then weakly focused onto the metasurface. The light was focused using a 0.055 NA objective, which was sufficient to confine the beam to a 200 μm wide diameter area while producing minimal non-normal electric field components at the device interface. A germanium detector attached to a computer-controlled goniometer measured the transmitted light intensity as a function of angle.

Supporting Information

Supporting Information is available from the Wiley Online Library or from the author.

Acknowledgements

J.A.F. supervised the study. D.S. and J.Y. performed the simulations. D.S. and S.D. performed the experiments. All authors contributed to experimental planning, data analysis, and writing the paper. The samples in this study were fabricated at the Stanford Nanofabrication Facility and Stanford Nano Shared Facility. The simulations were performed in the Sherlock computing cluster at Stanford University. This work was supported by the U.S. Air Force under Award Number FA9550-15-1-0161 and the Office of Naval Research under Award Number N00014-16-1-2630. D.S. was supported by the National Science Foundation (NSF) through the NSF Graduate Research Fellowship, and S.D. was supported by the Department of Defense through the National Defense Science and Engineering Graduate Fellowship Program.

Conflict of Interest

The authors declare no conflict of interest.

Keywords

blazed grating, inverse design, metasurfaces, multifunction, multimode

Received: July 3, 2017

Revised: July 31, 2017

Published online: October 16, 2017

- [1] P. Genevet, F. Capasso, *Rep. Prog. Phys.* **2015**, 78, 024401.
- [2] M. Khorasaninejad, W. T. Chen, R. C. Devlin, J. Oh, A. Y. Zhu, F. Capasso, *Science* **2016**, 352, 1190.
- [3] A. Arbabi, Y. Horie, A. J. Ball, M. Bagheri, A. Faraon, *Nat. Commun.* **2015**, 6, 7069.
- [4] N. M. Estakhri, V. Neder, M. W. Knight, A. Polman, A. Alù, *ACS Photonics* **2017**, 4, 228.
- [5] D. Sell, J. Yang, S. Doshay, K. Zhang, J. A. Fan, *ACS Photonics* **2016**, 3, 1919.
- [6] F. Ding, A. Pors, Y. Chen, V. A. Zenin, S. I. Bozhevolnyi, *ACS Photonics* **2017**, 4, 943.
- [7] W. Yue, S. Gao, S. S. Lee, E. S. Kim, D. Y. Choi, *Sci. Rep.* **2016**, 6, 29756.
- [8] A. Soni, S. Purohit, R. S. Hegde, *IEEE Photonics Technol. Lett.* **2017**, 29, 110.
- [9] N. Yu, F. Capasso, *Nat. Mater.* **2014**, 13, 139.
- [10] J. B. Mueller, N. A. Rubin, R. C. Devlin, B. Groever, F. Capasso, *Phys. Rev. Lett.* **2017**, 118, 113901.
- [11] E. Arbabi, A. Arbabi, S. M. Kamali, Y. Horie, A. Faraon, *Opt. Express* **2016**, 24, 18468.
- [12] M. Khorasaninejad, W. T. Chen, A. Y. Zhu, J. Oh, R. C. Devlin, D. Rousso, F. Capasso, *Nano Lett.* **2016**, 16, 4595.
- [13] U. Levy, H. C. Kim, C. H. Tsai, Y. Fainman, *Opt. Lett.* **2005**, 30, 2089.
- [14] W. T. Chen, K. Y. Yang, C. M. Wang, Y. W. Huang, G. Sun, I. D. Chiang, C. Y. Liao, W. L. Hsu, H. T. Lin, S. Sun, L. Zhou, *Nano Lett.* **2013**, 14, 225.
- [15] M. Khorasaninejad, A. Ambrosio, P. Kanhaiya, F. Capasso, *Sci. Adv.* **2016**, 2, 5.
- [16] E. Arbabi, A. Arbabi, S. M. Kamali, Y. Horie, A. Faraon, *Sci. Rep.* **2016**, 6, 32803.
- [17] E. Maguid, I. Yulevich, D. Veksler, V. Kleiner, M. L. Brongersma, E. Hasman, *Science* **2016**, 352, 1202.
- [18] B. Wang, F. Dong, Q. T. Li, D. Yang, C. Sun, J. Chen, Z. Song, L. Xu, W. Chu, Y. F. Xiao, Q. Gong, *Nano Lett.* **2016**, 16, 5235.
- [19] E. Arbabi, A. Arbabi, S. M. Kamali, Y. Horie, A. Faraon, *Optica* **2016**, 3, 628.
- [20] J. Ding, S. An, B. Zheng, H. Zhang, *Adv. Opt. Mater.* **2017**, 5, 1700079.
- [21] F. Aieta, M. A. Kats, P. Genevet, F. Capasso, *Science* **2015**, 347, 1342.
- [22] A. Y. Piggott, J. Lu, T. M. Babinec, K. G. Lagoudakis, J. Petykiewicz, J. Vučković, *Sci. Rep.* **2014**, 4, 7210.
- [23] A. Y. Piggott, J. Lu, K. G. Lagoudakis, J. Petykiewicz, T. M. Babinec, J. Vučković, *Nat. Photonics* **2015**, 9, 374.
- [24] C. M. Lalau-Keraly, S. Bhargava, O. D. Miller, E. Yablonovitch, *Opt. Express* **2013**, 21, 21693.
- [25] P. I. Borel, A. Harpøth, L. H. Frandsen, M. Kristensen, P. Shi, J. S. Jensen, O. Sigmund, *Opt. Express* **2004**, 12, 1996.
- [26] D. Sell, J. Yang, S. Doshay, R. Yang, J. A. Fan, *Nano Lett.* **2017**, 17, 3752.
- [27] J. Yang, D. Sell, J. A. Fan, *Ann. Phys.* **2017**, <https://doi.org/10.1002/andp.201700302>.
- [28] J. Yang, J. A. Fan, *Opt. Lett.* **2017**, 42, 3161.
- [29] S. J. Byrnes, A. Lenef, F. Aieta, F. Capasso, *Opt. Express* **2016**, 24, 5110.
- [30] V. Egorov, M. Eitan, J. Scheuer, *Opt. Express* **2017**, 25, 2583.
- [31] M. D. Huntington, L. J. Lauhon, T. W. Odom, *Nano Lett.* **2014**, 14, 7195.
- [32] F. Wang, J. S. Jensen, O. Sigmund, *J. Opt. Soc. Am. B* **2011**, 28, 387.
- [33] J. P. Hugonin, P. Lalanne, *Reticolo Software for Grating Analysis*, Institut d'Optique, Orsay, France **2005**.
- [34] J. Yang, C. Sauvan, T. Paul, C. Rockstuhl, F. Lederer, P. Lalanne, *Appl. Phys. Lett.* **2010**, 97, 061102.